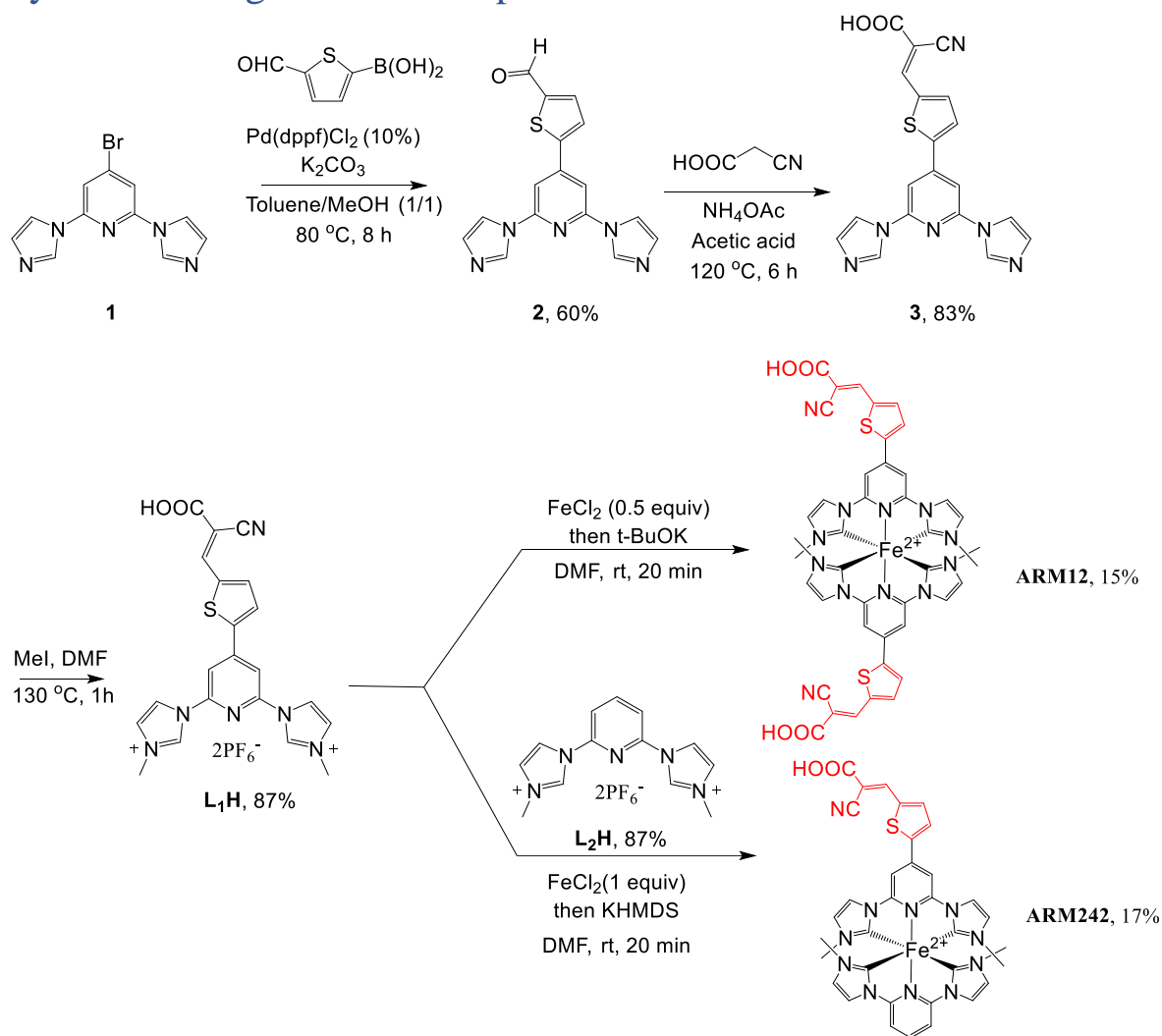


SUPPORTING INFORMATION

Synthesis of ligands and complexes.....	1
NMR spectra	3
Computational methods and data	10
Calculated opto-electronic properties of the dyes	12
Dye@TiO ₂ interface properties	16
Geometrical and electronic properties	16
Mulliken population analysis	17
Diabatic analysis.....	18
Electrode and cells preparation	20
Spectroscopic and Electrochemical methods and data	21
Absorption spectra of electrodes	22
Transient spectroscopy	23
Photovoltaic properties.....	25
References	26

Synthesis of ligands and complexes



Synthesis of 2. To a solution of **1**¹ (0.300 g, 1.03 mmol) in toluene (6 mL) was added a solution of 5-formylthiophene boronic acid (0.161 g, 1.03 mmol) and K₂CO₃ (0.428 g, 3.10 mmol) in methanol (6 mL). The mixture was purged with Argon for 20 min then PdCl₂(dppf) (0.076 g, 0.103 mmol) was added, and the solution was refluxed at 80 °C for 8 h. After completion of reaction, the reaction mixture was filtered through celite powder and washed with dichloromethane and methanol mixture. After evaporation of solvents, the residue was purified by column chromatography over silica gel using 7-9% methanol in dichloromethane as the eluent to give the product **2** as pale-yellow solid (0.200 g, 60 % yield). ¹H NMR (400 MHz, DMSO-d₆, δ ppm): 10.03 (s, 1H), 8.87 (s, 2H), 8.28-8.26 (m, 3H), 8.21 (d, *J* = 3.97 Hz, 1H), 8.10 (s, 2H), 7.19 (s, 2H). ESI-HRMS calcd for C₁₆H₁₂N₅OS *m/z* = 322.0757. Found: 322.0750. Due to poor solubility ¹³C NMR could not be recorded.

Synthesis of 3. To 10 mL of glacial acetic acid were added compound **2** (0.100 mg, 0.311 mmol) and cyanoacetic acid (0.053 mg, 0.622 mmol), and the solution was refluxed for 3 h in the presence of ammonium acetate (0.048 mg, 0.622 mmol). After cooling to room temperature, the mixture was poured into ice water. The precipitate was filtered, washed with distilled water, and dried under vacuum to get the desired compound **3** (0.100 g, yield 83 %). ¹H NMR (400 MHz, DMSO-

d_6 , δ ppm): 8.88 (s, 2H), 8.58 (s, 1H), 8.28 (s, 2H), 8.24 (d, J = 3.47 Hz, 1H), 8.16 (d, d, J = 3.66 Hz, 1H), 8.07 (s, 2H), 7.19 (s, 2H). ESI-HRMS calcd for $C_{19}H_{13}N_6O_2S$ m/z = 389.0815. Found: 389.0873. Due to poor solubility ^{13}C NMR could not be recorded.

Synthesis of L_1H . Compound **3** (0.093 g, 0.239 mmol) was charged in a 10 mL round bottomed flask and dissolved in 2 mL of DMF. Then added methyl iodide (16.4 μ L, 0.263 mmol) and heated the mixture at 130 °C for 1 h. Desired compound was precipitated upon addition of diethyl ether. Solid was collected by vacuum filtration and washed thrice with diethyl ether and dried under vacuum. Then the solid was dissolved in minimum amount of water+methanol (ca. 3 mL) and added saturated NH_4PF_6 solution followed by 2N HNO_3 until the solution became acidic ($pH \approx 2$) and stirred until the product precipitated. **L_1H** was collected by vacuum filtration and washed 3 times with water, diethyl ether and dried under vacuum (0.140 g, 83% yield). 1H NMR (400 MHz, CD_3CN , δ ppm): 9.59 (s, 2H, H_1), 8.53 (s, 1H, H_2), 8.32 (t, J = 1.95 Hz, 2H, H_3), 8.16 (s, 2H, H_4), 8.08 (d, J = 4.09 Hz, 1H, H_5), 8.00 (d, J = 4.14 Hz, 1H, H_6), 7.66 (t, J = 1.95 Hz, 2H, H_7), 4.05 (s, 6H, H_8). ^{13}C NMR (100 MHz, CD_3CN , δ ppm): 162.9 (C_1), 148.8 (C_2), 147.0 (C_3), 146.9 (C_4), 145.9 (C_5), 140.6 (C_6), 140.1 (C_7), 136.2 (C_8), 130.5 (C_9), 125.8 (C_{10}), 120.2 (C_{11}), 116.1 (C_{12}), 112.0 (C_{13}), 102.2 (C_{14}), 37.4 (C_{15}). ESI-HRMS calcd for $C_{21}H_{18}N_6O_2S$ m/z = 209.0600. Found: 209.0618.

Synthesis of $ARM12$. To a solution of **L_1H** (0.06 g, 0.084 mmol) in 2 mL of anhydrous DMF was added $FeCl_2$ (5.4 mg, 0.042 mmol) and degassed the mixture with Argon for 10 min. Then added $KHMDS$ (0.124 g, 0.677 mmol) to the above mixture at 0 °C and then slowly warmed to room temperature and stirred for 20 min. A saturated solution of NH_4PF_6 was added (10 ml) followed by addition of 2N HNO_3 until the solution becomes acidic ($pH \approx 2$) and the formed precipitate was collected by filtration. Then the crude was further purified on silica gel column chromatography using acetone/ H_2O/KNO_3 (sat) = 10: 3: 3 mixtures. The bluish-purple fraction was collected and after the evaporation of acetone, the left solution was treated with a saturated solution of NH_4PF_6 followed by addition of 2N HNO_3 until the solution becomes acidic ($pH \approx 2$). Affording the precipitation of the complex, it was then filtered, washed with distilled water followed by ether, and dried under vacuum. The isolated **$ARM12$** was obtained as a bluish powder (0.011 g, 15 % yield). 1H NMR (400 MHz, CD_3CN , δ ppm): 8.53 (s, 1H, H_1), 8.20 (d, J = 1.55 Hz, 2H, H_2), 8.13 (s, 2H, H_3), 8.09 (d, J = 3.85 Hz, 1H, H_4), 8.01 (d, J = 3.73 Hz, 1H, H_5), 7.05 (d, J = 1.71 Hz, 2H, H_6), 2.61 (s, 6H, H_7). ^{13}C NMR (100 MHz, CD_3CN , δ ppm): 200.5 (C_1), 163.3 (C_2), 154.9 (C_3), 148.9 (C_4), 146.9 (C_5), 142.6 (C_6), 140.7 (C_7), 138.9 (C_8), 129.3 (C_9), 127.5 (C_{10}), 117.4 (C_{11}), 116.5 (C_{12}), 102.9 (C_{13}), 101.7 (C_{14}), 35.5 (C_{15}). DEPT(^{13}C NMR): 146.8 (C_1), 140.5 (C_2), 129.2 (C_3), 127.3 (C_4), 117.3 (C_5), 102.8 (C_6), 35.3 (C_7). ESI-HRMS calcd for $C_{42}H_{32}FeN_{12}O_4S_2$ m/z = 444.0725. Found: 444.0740.

Synthesis of $ARM242$. To a solution of **L_1H** (0.07 g, 0.099 mmol) and ligand **L_2H^2** (0.052 g, 0.099 mmol) in 3 mL of anhydrous DMF was added $FeCl_2$ (0.013 g, 0.099 mmol) and degassed the mixture with Argon for 10 min and cooled the mixture to 0 °C. Then added $KHMDS$ (0.118 g, 0.593 mmol) to the above mixture at 0 °C and then slowly warmed to room temperature and stirred for 20 min. A saturated solution of NH_4PF_6 was added (10 ml) followed by addition of 2N HNO_3 until the solution becomes acidic ($pH \approx 2$) and the formed precipitate was collected by filtration. Then the crude was further purified on silica gel column chromatography using acetone/ H_2O/KNO_3 (sat) = 10: 3: 0.5 mixtures. The purple fraction was collected and after the

evaporation of acetone, the left solution was treated with a saturated solution of NH_4PF_6 followed by addition of 2N HNO_3 until the solution becomes acidic ($\text{pH} \approx 2$). Affording the precipitation of the complex, it was then filtered, washed with distilled water followed by ether, and dried under vacuum. The isolated **ARM242** was obtained as a purple powder (0.017 g, 17 % yield). ^1H NMR (400 MHz, CD_3CN , δ ppm): 8.48 (s, 1H, H_1), 8.23-8.17 (m, 3H, H_2 , H_3), 8.10-8.08 (m, 2H, H_4), 8.05 (d, $J = 4.18$ Hz, 1H, H_5), 8.01 (d, $J = 2.05$ Hz, 2H, H_6), 7.95 (d, $J = 4.18$ Hz, 1H, H_7), 7.74 (d, $J = 8.15$ Hz, 2H, H_8), 7.02-7.00 (m, 4H, H_9 , H_{10}), 2.57 (s, 6H, H_{11}), 2.52 (s, 6H, H_{12}). ^{13}C NMR (100 MHz, CD_3CN , δ ppm): 200.6 (C_1), 200.4 (C_2), 163.7 (C_3), 154.9 (C_4), 154.4 (C_5), 148.4 (C_6), 146.2 (C_7), 141.9 (C_8), 140.4 (C_9), 139.3 (C_{10}), 138.8 (C_{11}), 129.0 (C_{12}), 127.2 (C_{13}), 117.2 (C_{14}), 117.0 (C_{15}), 106.0 (C_{16}), 102.5 (C_{17}), 35.3 (C_{18}), 35.0 (C_{19}). DEPT(^{13}C NMR): 145.6 (C_1), 139.8 (C_2), 138.7 (C_3), 128.4 (C_4), 126.6 (C_5), 116.6 (C_6), 116.4 (C_7), 105.4 (C_8), 102.1 (C_9), 101.9 (C_{10}), 34.7 (C_{11}), 34.4 (C_{12}). ESI-HRMS calcd for $\text{C}_{34}\text{H}_{29}\text{FeN}_{11}\text{O}_2\text{S}$ $m/z = 355.5782$. Found: 355.5829.

NMR spectra

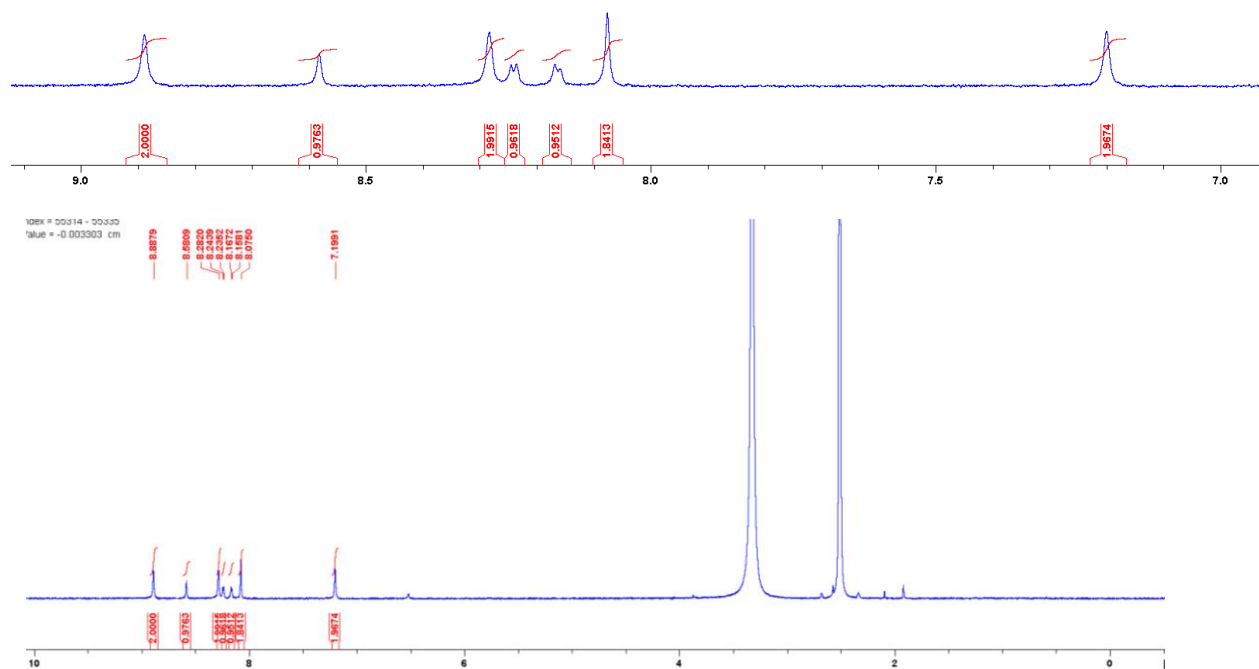


Figure S1: ^1H NMR spectra of compound **2**.

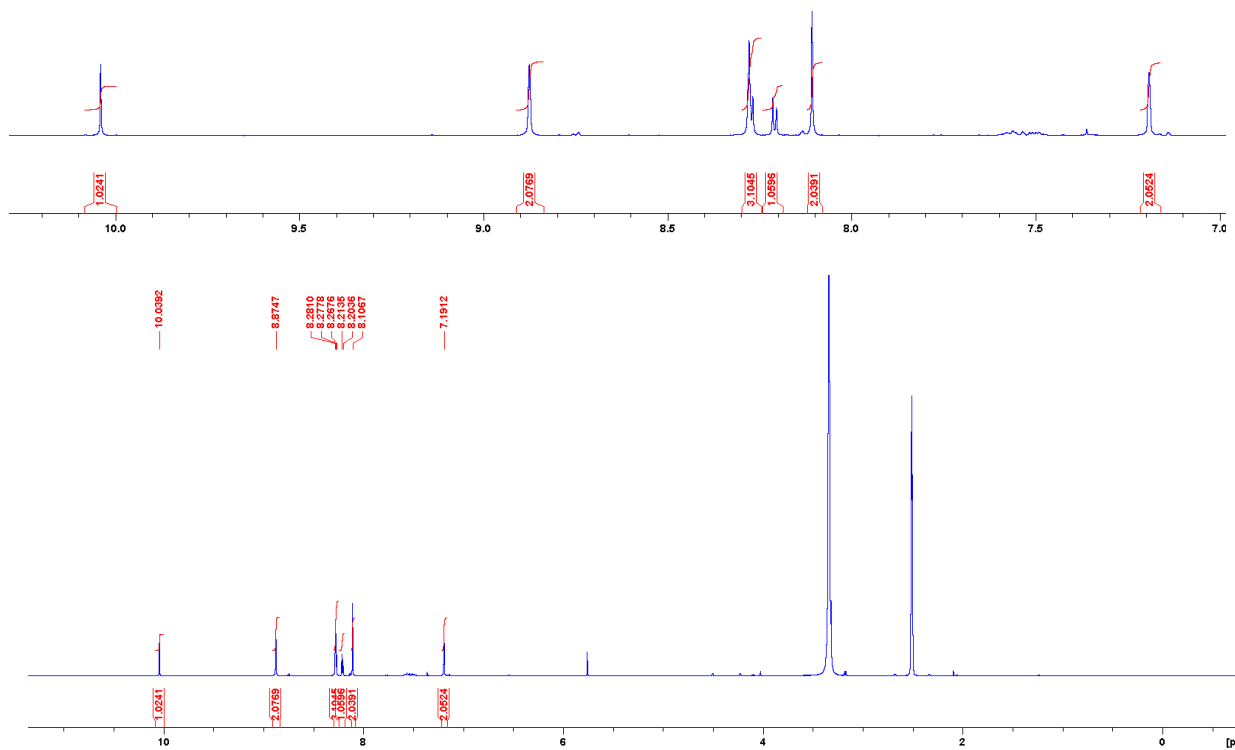
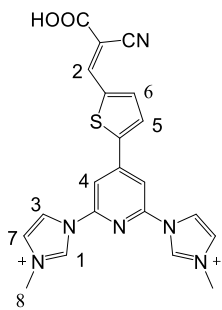


Figure S2: ^1H NMR spectra of compound 3.



^1H NMR (400 MHz, CD_3CN , δ ppm): 9.59 (s, 2H, H1), 8.53 (s, 1H, H2), 8.32 (t, $J=1.95$ Hz, 2H, H3), 8.16 (s, 2H, H4), 8.08 (d, $J=4.09$ Hz, 1H, H5), 8.00 (d, $J=4.14$ Hz, 1H, H6), 7.66 (t, $J=1.95$ Hz, 2H, H7), 4.05 (s, 6H, H8).

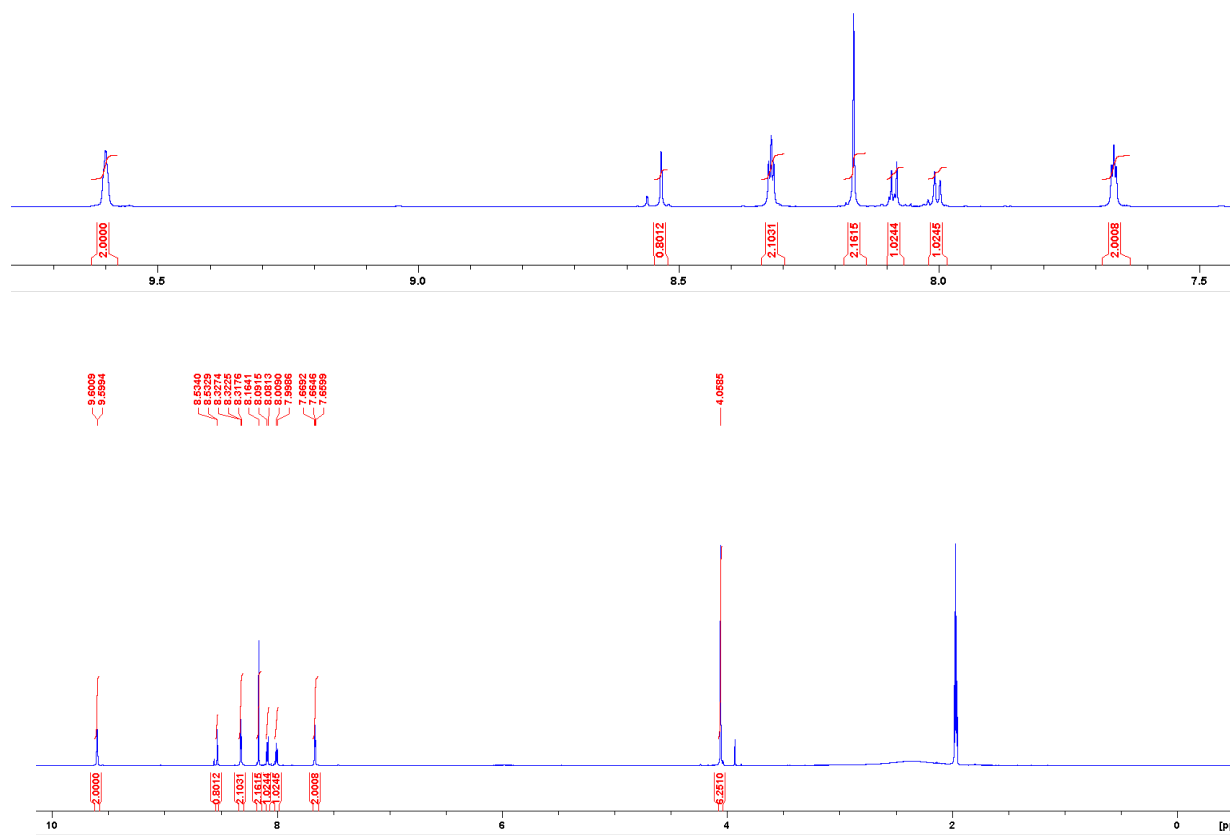
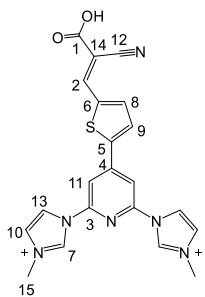


Figure S3: ^1H NMR spectra of compound **L1H**.



^{13}C NMR (100 MHz, CD_3CN , δ ppm): 162.9 (C1), 148.8 (C2), 147.0 (C3), 146.9 (C4), 145.9 (C5), 140.6 (C6), 140.1 (C7), 136.2 (C8), 130.5 (C9), 125.8 (C10), 120.2 (C11), 116.1 (C12), 112.0 (C13), 102.2 (C14), 37.4 (C15).

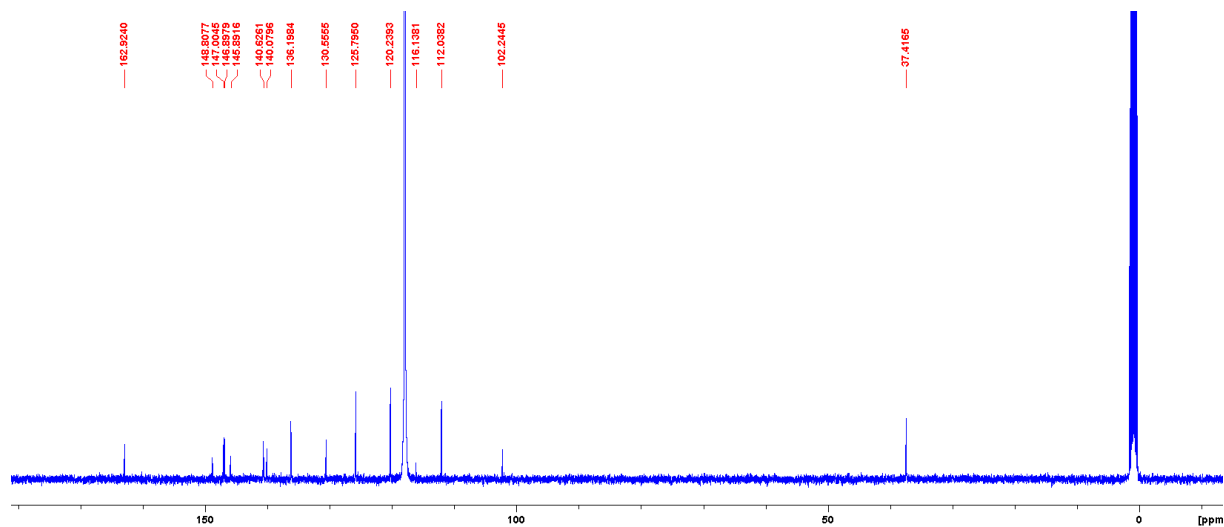


Figure S4 : ^{13}C NMR spectra of compound **L1H**.

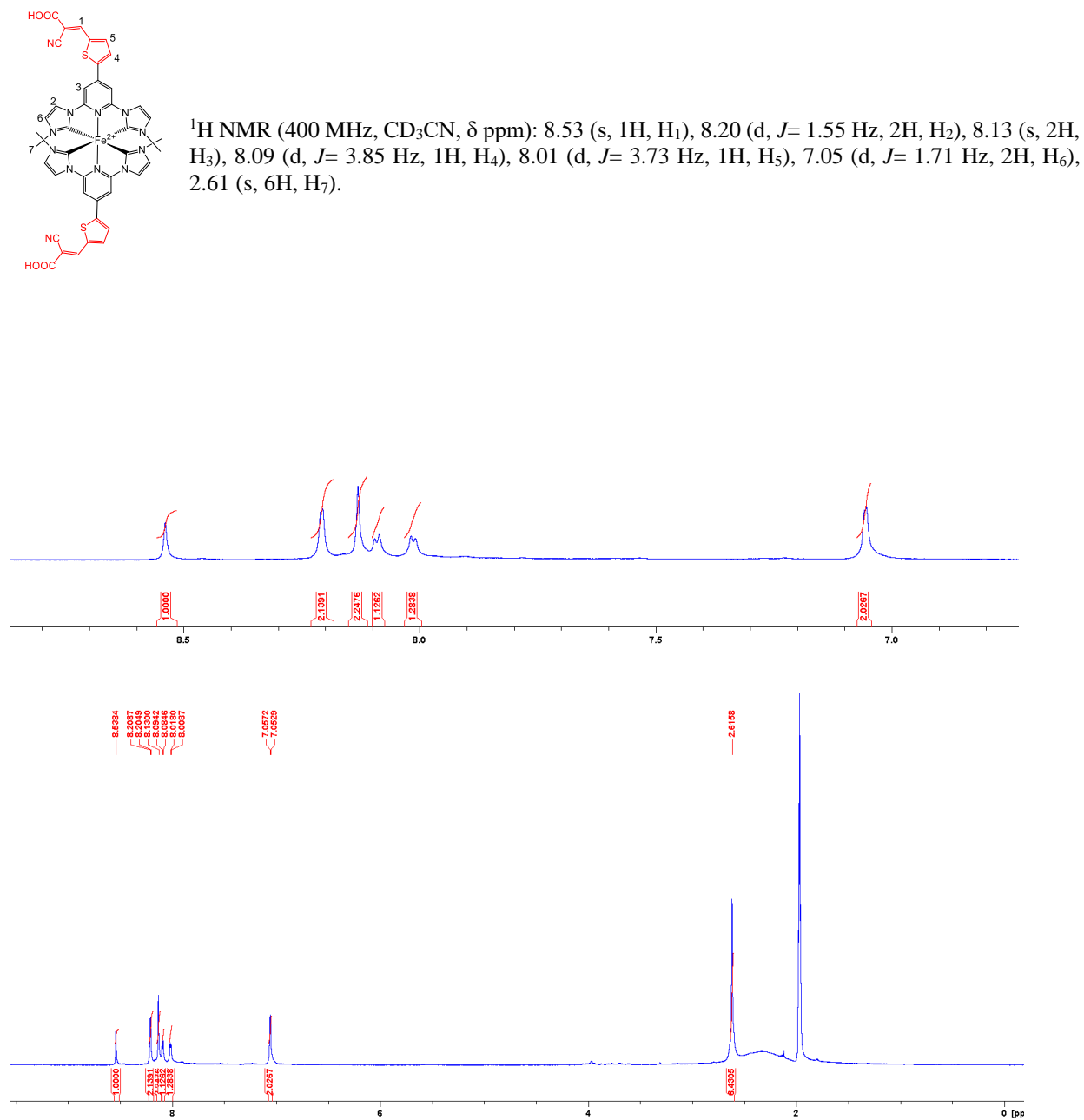
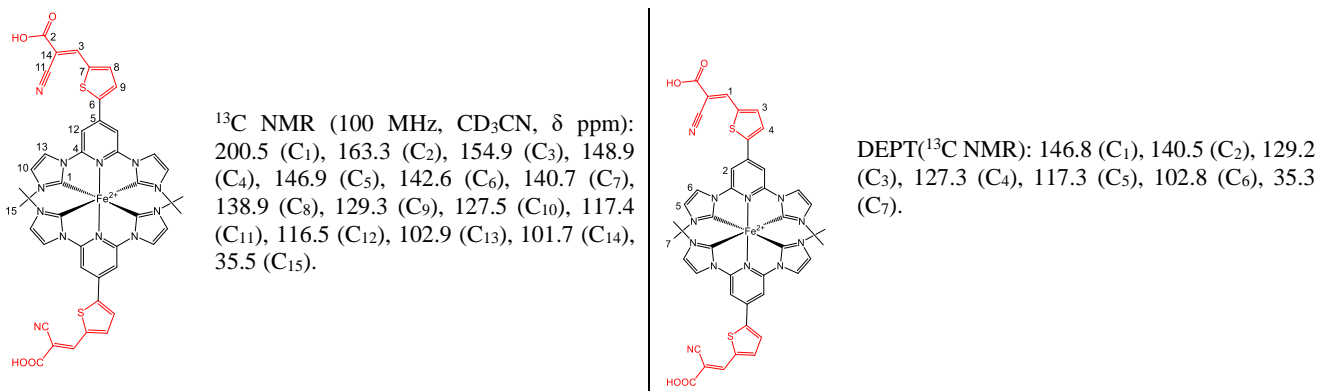


Figure S5: ¹H NMR spectra of ARM12.



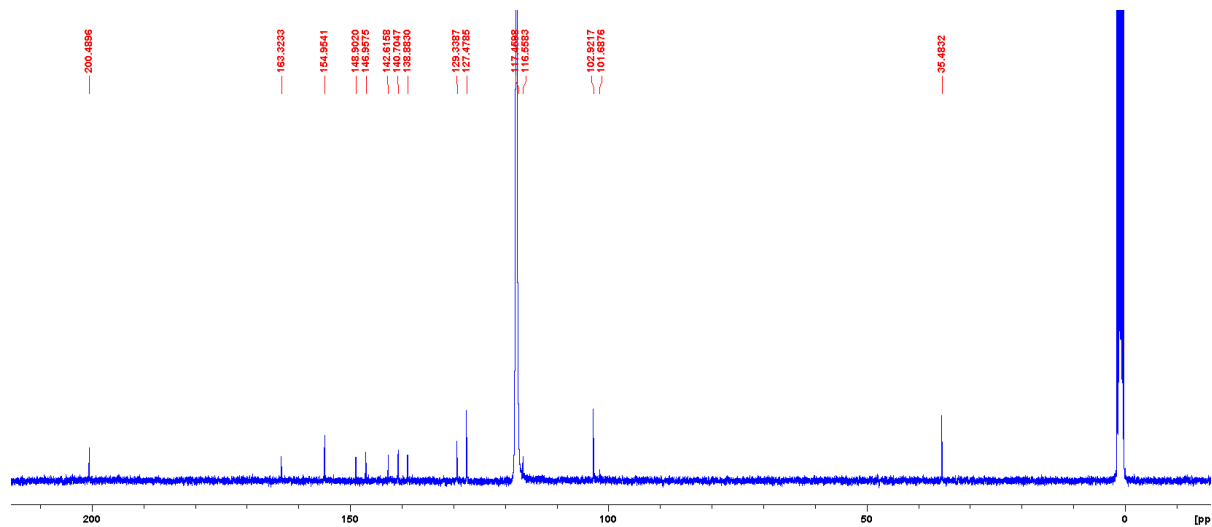


Figure S6: ^{13}C NMR spectra of ARM12.

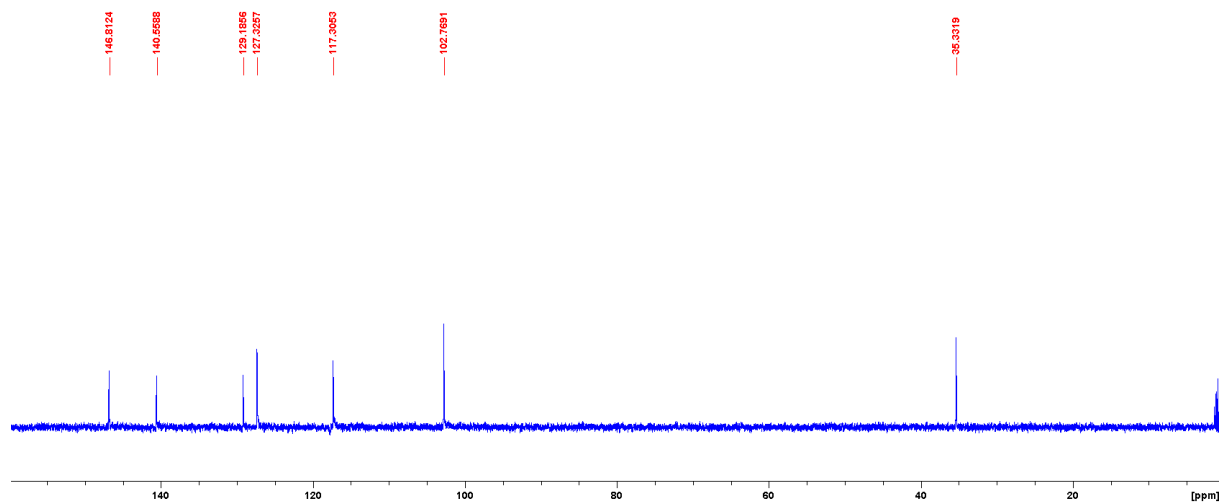
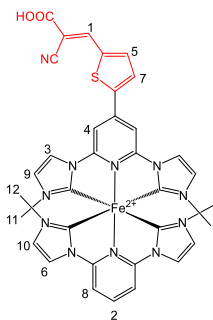


Figure S7: DEPT (^{13}C NMR) spectra of ARM12.



^1H NMR (400 MHz, CD_3CN , δ ppm): 8.48 (s, 1H, H1), 8.23-8.17 (m, 3H, H2, H3), 8.10-8.08 (m, 2H, H4), 8.05 (d, $J = 4.18$ Hz, 1H, H5), 8.01 (d, $J = 2.05$ Hz, 2H, H6), 7.95 (d, $J = 4.18$ Hz, 1H, H7), 7.74 (d, $J = 8.15$ Hz, 2H, H8), 7.02-7.00 (m, 4H, H9, H10), 2.57 (s, 6H, H11), 2.52 (s, 6H, H12).

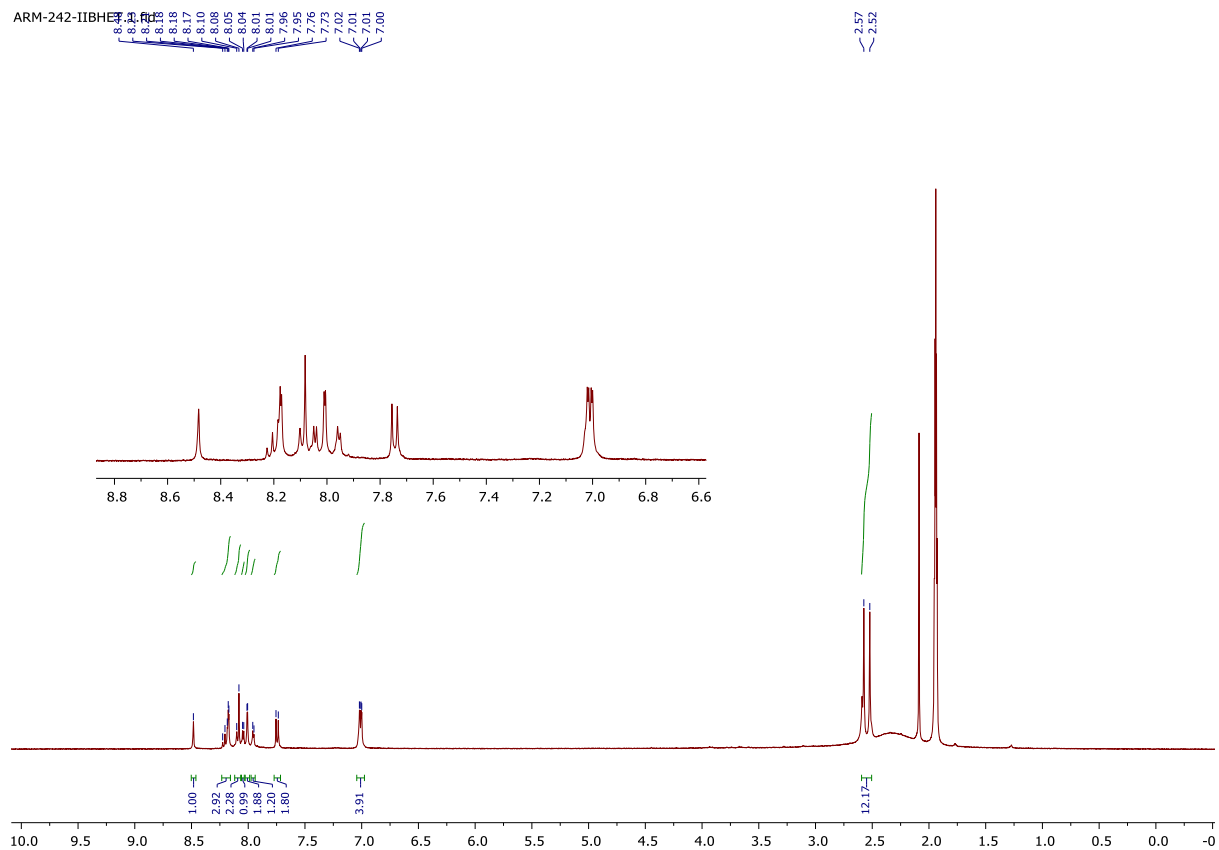
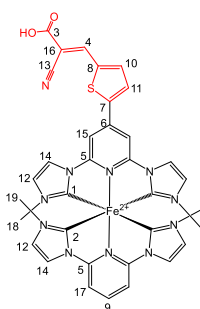
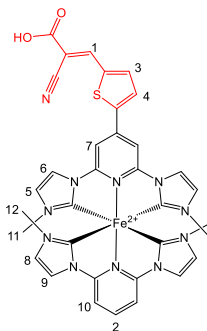


Figure S8: ^1H NMR spectra of ARM242.



^{13}C NMR (100 MHz, CD_3CN , δ ppm): 200.6 (C1), 200.4 (C2), 163.7 (C3), 154.9 (C4), 154.4 (C5), 148.4 (C6), 146.2 (C7), 141.9 (C8), 140.4 (C9), 139.3 (C10), 138.8 (C11), 129.0 (C12), 127.2 (C13), 117.2 (C14), 117.0 (C15), 106.0 (C16), 102.5 (C17), 35.3 (C18), 35.0 (C19).



DEPT(^{13}C NMR): 145.6 (C1), 139.8 (C2), 138.7 (C3), 128.4 (C4), 126.6 (C5), 116.6 (C6), 116.4 (C7), 105.4 (C8), 102.1 (C9), 101.9 (C10), 34.7 (C11), 34.4 (C12).

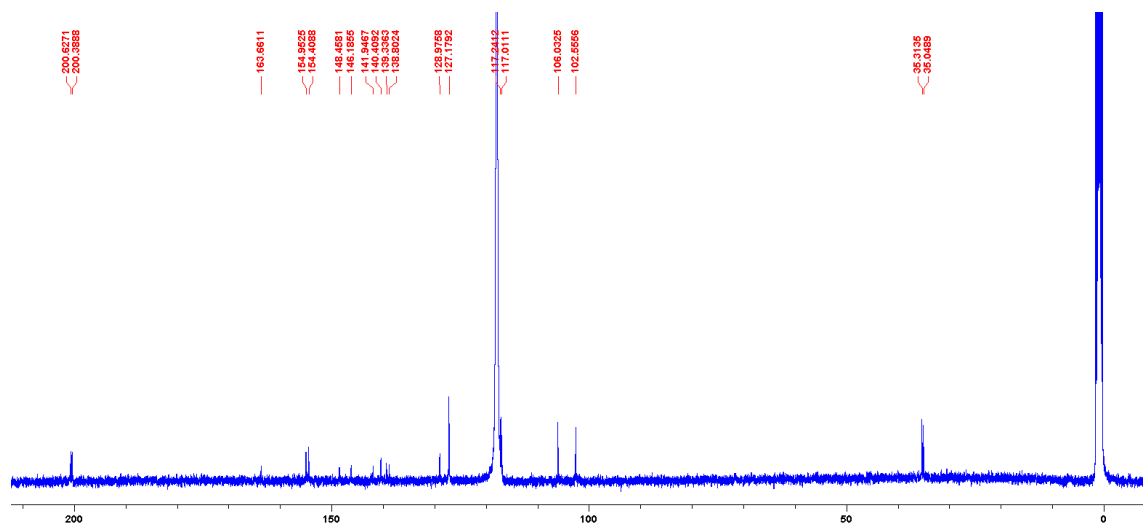


Figure S9: ^{13}C NMR spectra of **ARM242**.

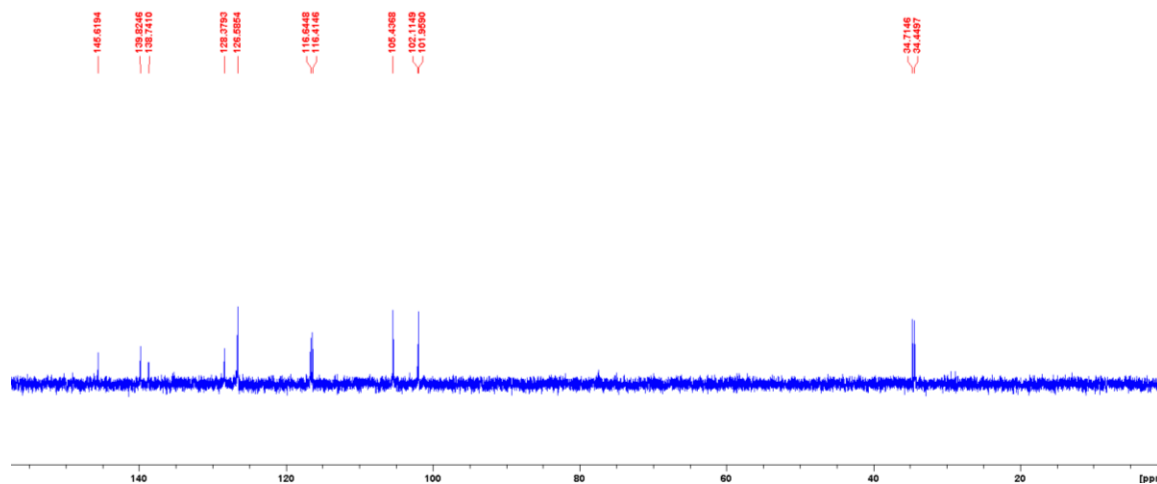


Figure S10: DEPT(^{13}C NMR) spectra of **ARM242**.

Computational methods and data

The computational strategy adopted here is similar to the one used in our previous works,^{1,3,4} which was successfully applied to rationalize the photovoltaic performances of Fe-NHC based DSSCs. The calculations of the isolated **ARM13** and **C1** were conducted in the Density Functional Theory (DFT) framework and its Time-dependent implementation (TD-DFT) within the modified B3LYP* functional⁵ (which possess a 15% of exact exchange fraction), and a 6-311G** basis sets. This computational approach has proved to accurately reproduce the opto-electronic properties of Fe(II) complexes in the past.⁶⁻⁸ Nevertheless, the introduction of the cyanoacrylic group in this

new series of dyes, substantially increases the CT character of the MLCT states, in principle, requiring a larger amount of non-local exchange in the functional. Preliminary calculations (see Tables S1 and S2) showed, indeed, that the standard B3LYP functionals⁹ (20% of exact exchange correlation) yielded to a more accurate estimation of the MLCT band energies with respect to B3LYP* for **ARM12** and **ARM242**. The methanol solvent environment was considered by means of the Conductive Polarizable Continuum Model (CPCM).¹⁰ The dye geometries were first optimized in their ground state (GS), followed by the computation of their vertical excitations at the TD-DFT level. All these calculations were carried out within the Gaussian16 program package.¹¹

For the investigation of the dye@TiO₂ interfaces we relied on a (TiO₂)₈₂ cluster model,¹² obtained by exposing the bulk anatase to the 101 direction.¹² The dyes were attached in a bidentate fashion to the TiO₂ surface and the resulting systems were fully relaxed at the DFT level by employing the Perdew–Burke–Ernzerhof (PBE) functional with D3 Grimme’s dispersion correction,^{13,14} and the COnductor-like Screening MOde (COSMO) model¹⁵ to model the solvent environment (acetonitrile in this case), as it is implemented in the Amsterdam Density Functional (ADF) package.¹⁶ Double/Triple Zeta Polarized (DZP/TZP) basis sets were used for C, N, H, S, O, Mg/Fe, Ti atoms, respectively. As we demonstrated in our previous studies,¹ one needs to consider the explicit effect of the Mg²⁺ cations adsorbed on the TiO₂ surface to recover the proper CT directionality towards the semiconductor for the homoleptic Fe-NHC sensitizers. In this context, we relied on the same procedure as the one established before,¹ where the geometries of the Mg²⁺ cation on the ARM12@TiO₂ system were optimized following the same computational strategy as the one used for the bare dye@TiO₂ interface. Note that, we systemically set up the same position for the Mg²⁺ cation on the surface for all the models, with the closest distances to the oxygen atoms of the TiO₂ surface amounting to 2.15, 2.24 and 2.59 Å, as depicted in Figure 10. In a final step, the electronic structure of the resulting dye@TiO₂-Mg system was computed within the same methodology as the one described above for the isolated dyes. The injection/recombination properties at dye@TiO₂-Mg interface were estimated by resorting in the diabatic analysis developed by Thoss and co-workers.¹⁷ Within this method, the diabatic *k* and *d* states for the dye (donor) and the TiO₂-Mg (acceptor) manifolds, respectively; are calculated by localizing their molecular orbitals (MOs) into their corresponding moieties, thus resulting in a Fock matrix where the diagonal elements contains the localized *k* and *d* state energies, while the off-diagonal terms corresponds to the dye/semiconductor V_{kd} couplings. Then, by resorting to the Fermi-golden rule, the injection rates can be estimated as follows:

$$k_{inj} = \frac{2\pi}{\hbar} \sum_k |V_{kd}|^2 \rho(\varepsilon_k)$$

Where $\rho(\varepsilon_k)$ is the TiO₂-Mg partial density of states (DOS), and the $|V_{kd}|^2 \rho(\varepsilon_k)$ product represents the so-called probability distribution $\Gamma(\varepsilon_k)$.

Calculated opto-electronic properties of the dyes

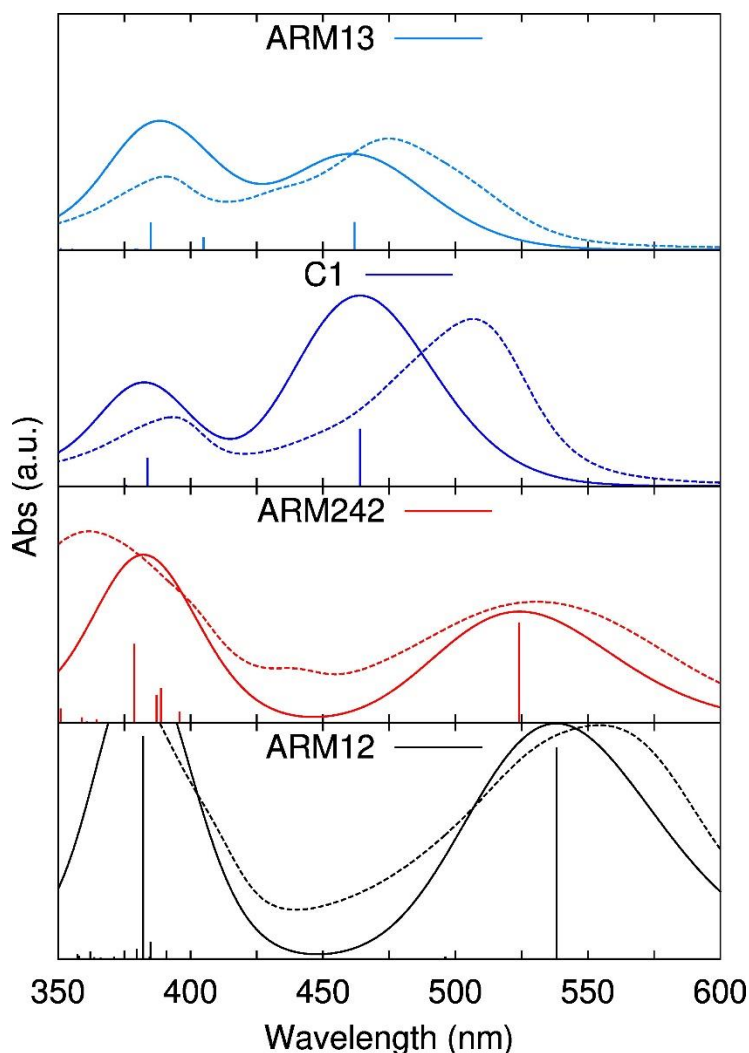


Figure S11: Simulated (continuous) and experimental (dashed lines) UV-Vis spectra for **ARM13** (light blue), **C1** (dark blue), **ARM242** (red) and **ARM12** (black color), as represented from the top to the bottom panels. Vertical bars represent the oscillator strength of the vertical transitions conforming the spectra, which was built by employing a half-width at full-length of 0.15 eV. The absorption intensity of **ARM13** and **C1** has been multiplied by a factor of 3 for the sake of a clearer representation. Note that the **ARM13/C1** and **ARM242/ARM12** simulated spectra have been estimated at the TD-B3LYP*/6-311G(d) and TD-B3LYP/6-311G(d) levels of theory. The characteristics of the main transitions in the VIS region are reported in the rows highlighted with yellow color in Tables S1 and S2.

Table S1 State number (n), excitation energies (E_x), wavelengths (λ), oscillator strengths (f), major contributions and related percentage (%) of the main transitions in the visible region, as estimated at the TD-B3LYP*/6-311G(d) level of theory. Transitions related with MLCT excitations are marked with orange color.

<i>dye</i>	n	E_x (eV)	λ (nm)	f (a.u.)	<i>Transition</i>	%
ARM13	4	2.69	461	0.148	H-2→L	63.4
					H→L+2	27.6
	9	3.22	385	0.150	H→L+3	55.0
					H→L+2	40.5
ARM242	3	2.16	575	0.496	H-1→L	69.3
					H→L+3	9.5
	11	3.14	395	0.434	H-3→L	50.0
					H-1→L+2	40.8
12	3.15	394	0.267	H→L+4	49.4	
				H→L+3	30.3	
C1	5	2.67	464	0.324	H-2→L+1	44.5
					H-1→L	44.2
	9	3.23	384	0.161	H→L+3	69.5
					H-1→L	7.2
ARM12	5	2.10	590	1.062	H-2→L+1	49.9
					H-1→L	49.3
	16	3.12	398	1.338	H-4→L	41.7
					H-3→L+1	41.1

Table S2 State number (n), excitation energies (E_x), wavelengths (λ), oscillator strengths (f), major contributions and related percentage (%) of the main transitions in the visible region, as estimated at the TD-B3LYP/6-311G(d) level of theory. Transitions related with MLCT excitations are marked with orange color.

<i>dye</i>	n	E_x (eV)	λ (nm)	f (a.u.)	<i>Transition</i>	%
ARM13	4	2.84	437	0.161	H-1→L	49.7
					H→L+2	25.7
	12	3.46	358	0.143	H→L+2	57.4
					H→L+3	38.6
ARM242	3	2.37	524	0.566	H-1→L	68.9
					H→L+3	9.7
	9	3.19	389	0.194	H-4→L	45.3
					H-3→L	32.2
11	3.27	379	0.443	H-3→L	57.6	
				H-2→L+1	24.3	
C1	5	2.83	438	0.325	H-2→L+1	42.8
					H-1→L	42.5
	12	3.47	357	0.161	H→L+3	69.7

					H-2→L+1	5.6
ARM12	5	2.30	538	1.193	H-2→L+1	49.8
					H-1→L	48.6
	13	3.24	382	1.256	H-3→L+1	46.1
					H-4→L	42.7

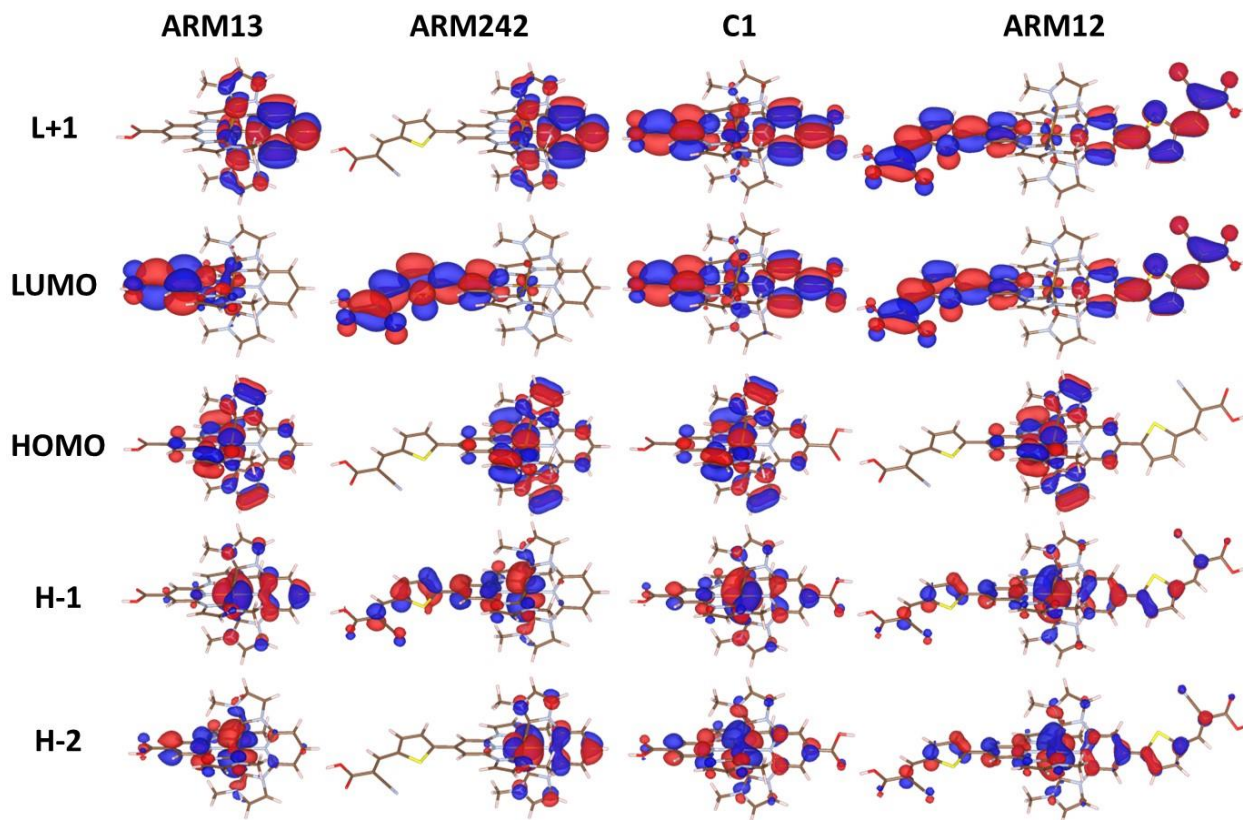


Figure S12: MO shapes of the levels involved in the main transition composing the MLCT bands of **ARM13**, **ARM242**, **C1** and **ARM12** and (from the left to the right part), as indicated in Tables S1 and S2. The corresponding energy values of these orbitals calculated by B3LYP* and B3LYP functionals are reported in Tables S3 and S4, respectively. The isovalue used to plot the isodensities was 0.02 a.u.

Table S3: Kohn-Sham (KS) energies and corresponding HOMO-LUMO gaps in eV for the energy levels plotted in Figure S3, as estimated by employing the modified B3LYP* hybrid functional.

<i>dye</i>	H-2	H-1	HOMO	LUMO	L+1	$(E_g)_{dye}$
ARM13	-6.04	-6.03	-5.68	-2.96	-2.30	2.72
C1	-6.14	-6.14	-5.77	-3.00	-3.00	2.77
ARM242	-5.98	-5.91	-5.65	-3.54	-2.28	2.11
ARM12	-5.96	-5.96	-5.71	-3.54	-3.54	2.16

Table S4: KS energies and corresponding HOMO-LUMO gaps in eV for the for the energy levels plotted in Figure S3, as estimated by employing the standard B3LYP hybrid functional.

<i>dye</i>	H-2	H-1	HOMO	LUMO	L+1	$(E_g)_{\text{dye}}$
ARM13	-6.35	-6.34	-5.95	-2.83	-2.14	3.12
C1	-6.45	-6.44	-6.03	-2.87	-2.87	3.17
ARM242	-6.29	-6.20	-5.91	-3.43	-2.12	2.48
ARM12	-6.24	-6.24	-5.96	-3.43	-3.43	2.53

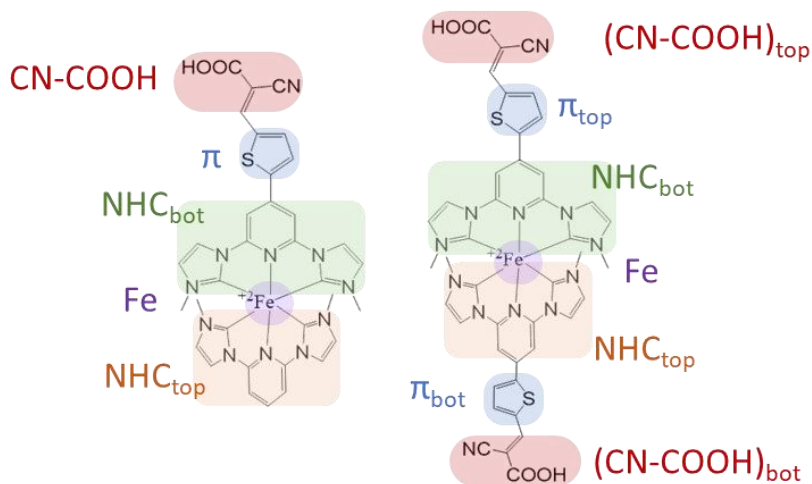


Figure S13: Schematic representation of the different fragments employed for the transition density matrix CT analysis conforming the heteroleptic (left) and homoleptic (right) dyes.

Table S5: Calculated fraction of holes (h^+) and electrons (e^-) localized along the different fragments conforming the heteroleptic dyes, as represented Figure S2 left: carboxylic anchoring group (CN-COOH), thiophene bridge (π), bounded ligand (NHC_{bot}), metal cation (Fe), and unbounded ligand (NHC_{top}).

<i>frag</i>	ARM13		ARM242	
	h^+	e^-	h^+	e^-
NHC_{top}	0.091	0.057	0.086	0.026
Fe	0.730	0.078	0.661	0.038
NHC_{bot}	0.173	0.709	0.153	0.313
π	-	-	0.071	0.309
CN-COOH	0.009	0.160	0.034	0.309

Table S6: Calculated fraction of holes (h^+) and electrons (e^-) localized along the different fragments conforming the homoleptic dyes, as represented in Figure S2 right: bounded carboxylic anchoring group

(CN-COOH_{bot}), bounded thiophene bridge (π_{bot}), bounded ligand (NHC_{bot}), metal cation (Fe), unbounded ligand (NHC_{top}), unbounded thiophene bridge (π_{top}), and carboxylic anchoring moieties (CN-COOH_{top}).

<i>frag</i>	C1		ARM12	
	h^+	e^-	h^+	e^-
CN-COOH _{top}	0.005	0.092	0.019	0.152
π_{top}	-	-	0.042	0.153
NHC _{top}	0.121	0.373	0.116	0.178
Fe	0.749	0.071	0.646	0.037
NHC _{bot}	0.121	0.374	0.116	0.177
π_{bot}	-	-	0.042	0.152
CN-COOH _{bot}	0.005	0.092	0.019	0.151

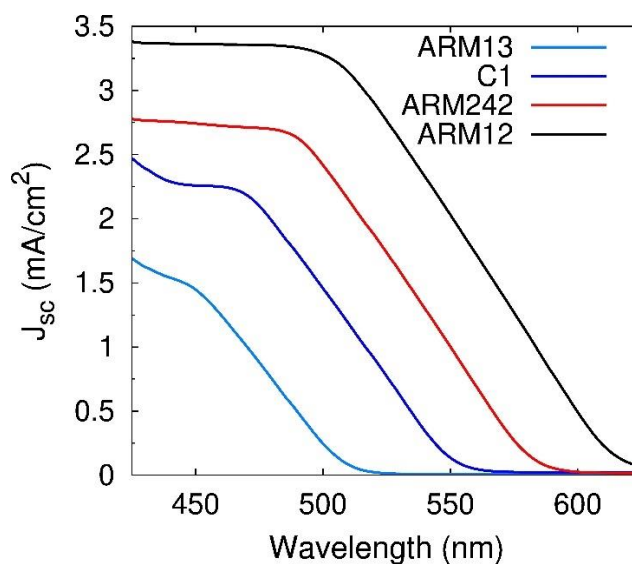


Figure S14: Calculated J_{sc} (mA/cm²) curves for the isolated dyes as computed from their simulated absorption spectra.

Dye@TiO₂ interface properties

Geometrical and electronic properties

Table S7: Geometrical properties dye@TiO₂ systems: anchoring bonding lengths in Å and tilted angles (θ) in degrees, as represented in Figure 10.

dye@TiO ₂	d(O-Ti) ₁	d(O-Ti) ₂	θ (°)
ARM13/C1	2.208	2.086	66.92
ARM242/ARM12	2.257	1.985	74.03

Table S8: Magnitude of the dipoles in the normal surface direction in Debyes (D) for the dye@TiO₂ systems.

dye@TiO ₂	μ_{\perp} (D)
ARM13	4.7
C1	2.7
ARM242	32.3
ARM12	35.0

Mulliken population analysis

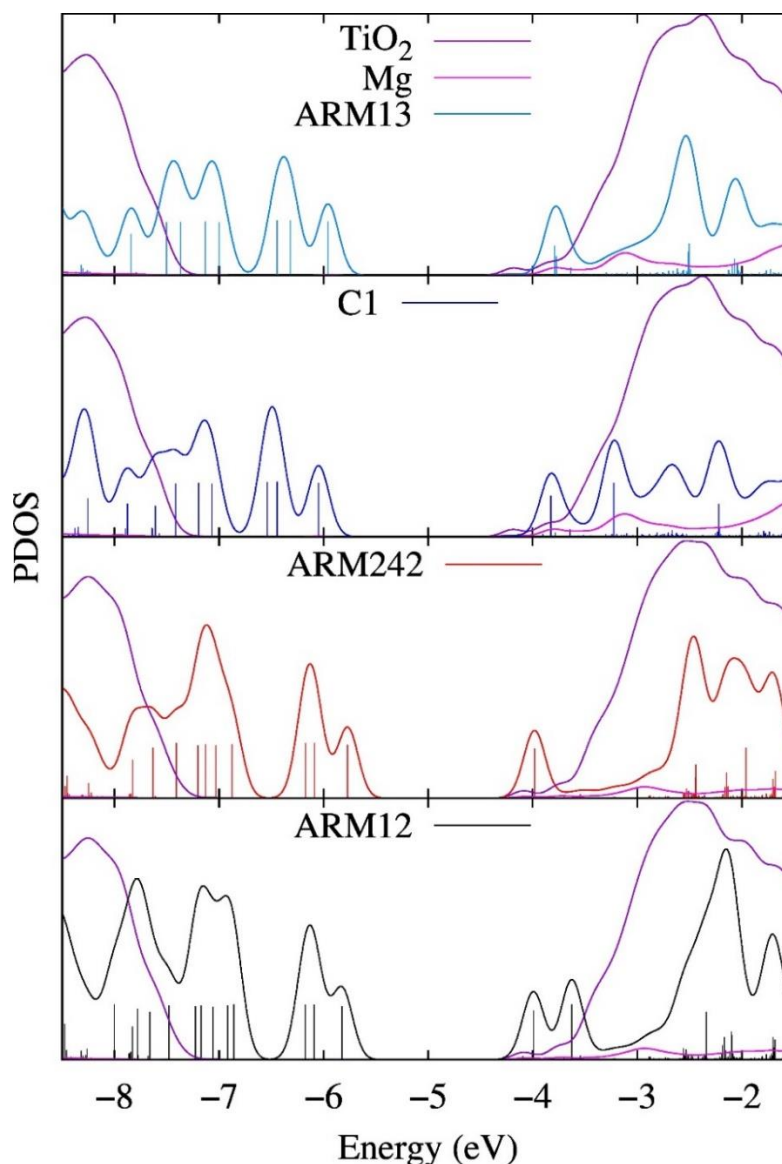


Figure S15: Projected Density of States (PDOS) of dye@TiO₂-Mg systems along the **ARM13** (bright blue), **C1** (dark blue), **ARM242** (red) and **ARM12** (black) dyes, TiO₂ surface (purple) and Mg²⁺ cation (magenta); as calculated by Mulliken population analysis. For visualisation purposes, only the vertical bars of the dye's PDOS are represented here and the TiO₂ DOS intensity has been divided by a factor of 10.

Table S9: Dye's FMO and TiO₂-Mg band edge energies in eV, and corresponding energy gaps as extracted for the states with a larger extent of delocalization along the dye/semiconductor blocks, from the Mulliken population analysis represented in Figure S14.

dye	TiO ₂ -Mg
-----	----------------------

dye@TiO ₂ -Mg	H-2	H-1	HOMO	LUMO	L+1	(E _g) _{dye}	VBM	CBM	(E _g) _{TiO₂}
ARM13	-6.44	-6.32	-5.96	-3.79	-2.50	2.17	-7.46	-4.19	3.27
C1	-6.54	-6.44	-6.05	-3.83	-3.23	2.22	-7.46	-4.19	3.27
ARM242	-6.17	-6.09	-5.77	-3.98	-2.44	1.79	-7.40	-4.09	3.30
ARM12	-6.17	-6.09	-5.82	-3.99	-3.63	1.83	-7.40	-4.09	3.30

Table S10: Dye's FMO and TiO₂ band edge energies in eV, and corresponding energy gaps as extracted for the states with a larger extent of delocalization along the dye/semiconductor blocks, from the Mulliken population analysis obtained by employing the standard B3LYP functional.

dye@TiO ₂ -Mg	<i>dye</i>						TiO ₂ -Mg			
	H-2	H-1	HOMO	LUMO	L+1	(E _g) _{dye}	VBM	CBM	(E _g) _{TiO₂}	
ARM242	-6.45	-6.36	-6.00	-3.86	-2.28	2.14	-7.69	-3.94	3.76	
ARM12	-6.43	-6.34	-6.05	-3.87	-3.52	2.18	-7.69	-3.94	3.76	

Diabatic analysis

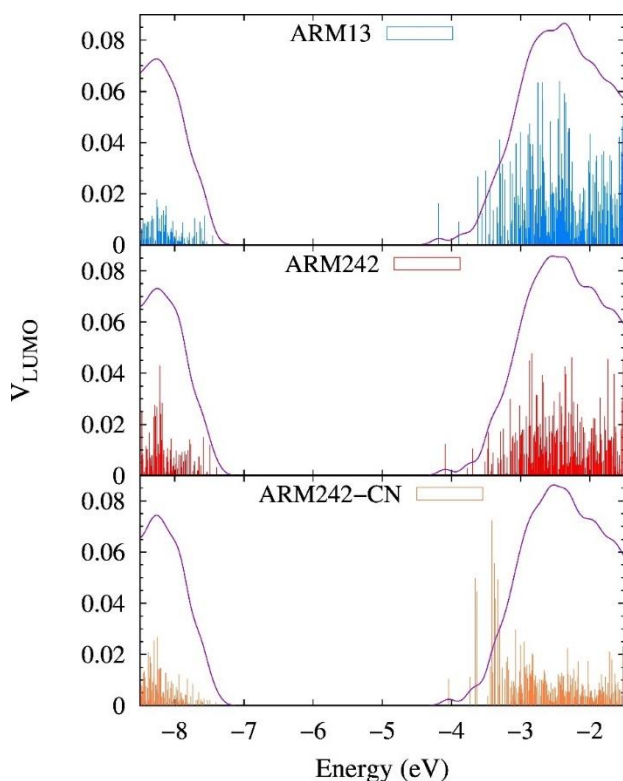


Figure S16: Electronic coupling V between the LUMOs of the heteroleptic ARM13 (bright blue), ARM242 (red) and ARM242-CN (orange) dyes; and the states of the TiO₂-Mg surface (vertical bars) together with the diabatic TiO₂ DOS (continuous purple lines).

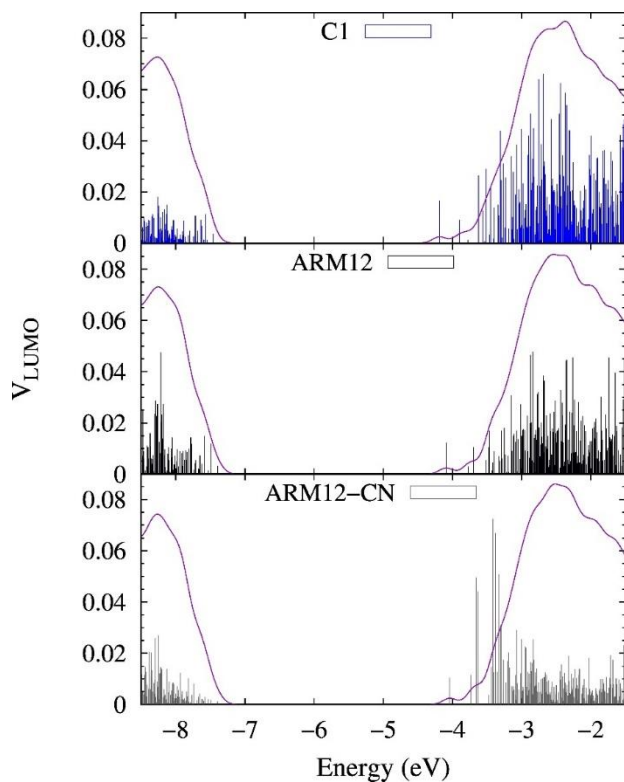


Figure S17: Electronic coupling V between the LUMOs of the homoleptic **C1** (dark blue), **ARM12** (black) and **ARM12-CN** (grey) dyes; and the states of the TiO_2 -Mg surface (vertical bars) together with the diabatic TiO_2 DOS (continuous purple lines).

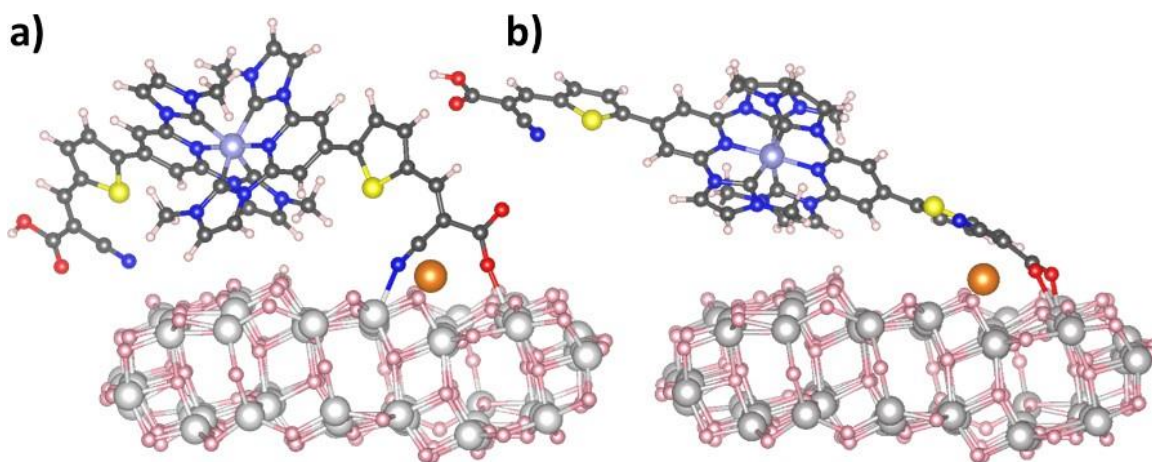


Figure S18: Comparison of the lateral view of the optimized structure of the a) **ARM12-CN@Mg-TiO₂** and the b) **ARM12@Mg-TiO₂** systems.

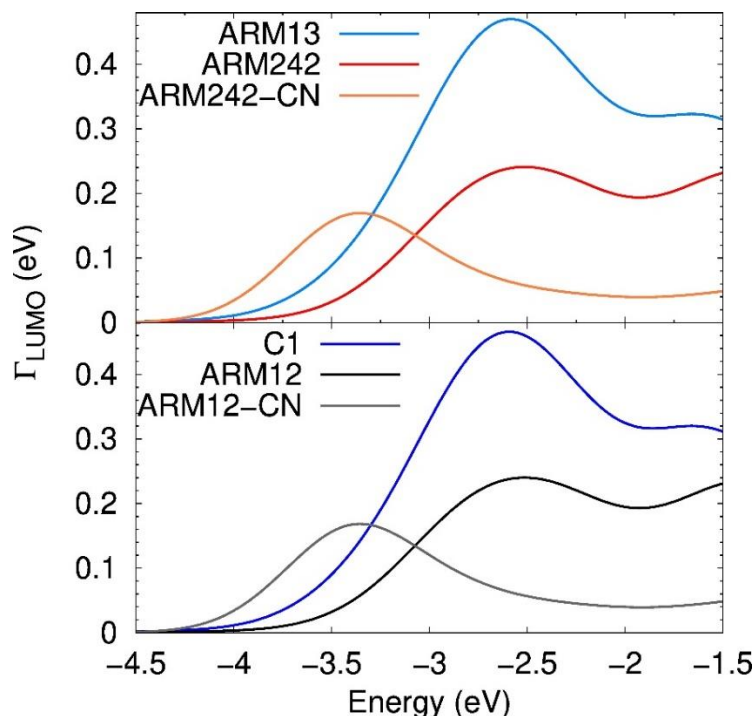


Figure S19: Probability distribution $\Gamma(\epsilon)$ for electron injection from the LUMO of the heteroleptic (top panel) and homoleptic (bottom panel) dyes to the TiO_2 .

Electrode and cells preparation

99.995% Lithium trifluoromethanesulfonate (LiOTf), 97% Magnesium trifluoromethanesulfonate ($\text{Mg}(\text{OTf})_2$), Guanidinium thiocyanate (GuNCS) $\geq 97\%$, Tetrabutylammonium iodide (TBAI) ≥ 98 , 1-Methyl-3-propylimidazolium Iodide (PMII) $\geq 98\%$, ACS grade I_2 $\geq 99.8\%$, , 3,4-Ethylenedioxythiophene (EDOT) 97%, Alconox, Titanium(IV) isopropoxide ($\text{Ti}(\text{OiPr})_4$), and solvents (anhydrous Acetonitrile (ACN) 99.8%, ACS grade 2-propanol $\geq 99.8\%$, 99.9% 1-butanol and anhydrous methanol 99.8%) were bought from Sigma-Aldrich and used without further purification. Magnesium iodide (MgI_2) $> 99\%$ and ultra dry LiI 99.999% were purchased from Fluka, LiClO_4 $\geq 99\%$ was bought from Acros organics. 1-Methyl-3-propylimidazolium trifluoromethanesulfonate (PMIOTf) was purchased from Tokyo Chemical Industry (TCI). FTO TEC-7 was obtained from NSG. Surlyn 25, Ti-nanoxide T/SP and Ti-nanoxide R/SP pastes were bought from Solaronix. ZrO_2 paste was prepared according to previously reported procedures.^{18,19}

The Fluorine Thin Oxide (FTO) slides were cleaned by subsequent dipping and sonication in 1% Alconox solution and 2-propanol for 10 min each time followed by an annealing treatment of 20 min at 450 °C. A compact blocking underlayer was fabricated by spin coating a 0.3 M $\text{Ti}(\text{IV})(\text{OiPr})_4/1$ -butanol solution (10 sec at 1000 rpm and 20 sec at 2000 rpm) followed by a sintering step at 500°C for 15 min. The active mesoporous TiO_2 films was cast by doctor blading technique between to two 3M scotch tape slides disposed at 5 mm of distance and sintered with the following temperature program: from RT to 120°C at 10°C/min, from 120°C to 450°C at 11°C/min, rest at 450°C for 30 min, ramp step to 500°C at 5°C/min and rest at 10 min at 500°C. The procedure related to the preparation of the active mesoporous titania film was repeated up to

3 times to increase the thickness of the substrate. A final TiCl_4 treatment was realized by drop casting followed by slow hydrolysis of 0.4M TiCl_4 /water solution in a closed chamber for 12h at room temperature. The films were then washed with deionized water, dried with warm air and annealed for 30 min at 450°C . The scattering top layer was obtained with the same procedure employed to obtain the mesoporous active TiO_2 by using a reflective paste (Ti-nanoxide R/SP, Solaronix) followed by the sintering process described above. The ZrO_2 films were prepared in a similar fashion, the paste was cast by doctor blading technique on cleaned FTO between two 3M scotch tape slides and sintered at 500°C for 30 min.

The dyes were chemisorbed on TiO_2 or ZrO_2 films by using 0.2 mM dye/0.04 mM chenodeoxycholic (CDCA) in acetonitrile solution for **C1** and in 1:1 acetonitrile:methanol solutions for **ARM12** and **ARM242**.

The PEDOT-based counter electrodes were fabricated by electropolymerization of a 10^{-2} EDOT/ 10^{-1} M LiClO_4 /ACN solution in CV by scanning the potential from 0 to 1.6 V Vs SCE at a scan rate of 50 mVs^{-1} . A cleaned FTO was used as working electrode, cofacially assembled at a distance of 2.3 mm from a titanium sheet ($A = 4 \text{ cm}^2$) as counter electrode while a double jacket SCE served as reference.

Cells were fabricated in an open configuration by confining the electrolyte inside a delimited area generated by a thermoplastic Surlyn 25 spacer. The photoanode and the counterelectrode were kept together with two clamps. Cells were filled with our customized electrolyte¹ composed as follow: 0.1 M LiI, 0.6 M PMII, 0.1 M I_2 , 0.1 M MgI_2 , 0.1 M GuNCS, 0.1 M TBAI in acetonitrile.

Spectroscopic and Electrochemical methods and data

Absorption spectra of the Fe(II)NHC sensitized photoanodes were recorded in transmission mode with an Agilent Carry 300 UV-Vis spectrophotometer, against an identical undyed TiO_2 electrode as a reference. The spectra of the opaque scattering photoanodes were recorded in diffuse reflectance mode with a JASCO V-570 spectrophotometer with an integrating sphere. The electrodes were illuminated through the FTO side.

Thin semiconductor films, either made of TiO_2 or ZrO_2 and modified with the Fe(II)NHC complexes were employed as working electrodes for cyclic voltammetry (CV) analysis, in a three-electrode cell with a platinum wire as counter-electrode and a Saturated Calomel Electrode (SCE) reference electrode. The experiments were recorded with a PGSTAT 302N potentiostat, with scan rate of 20 mVs^{-1} in 0.1M LiClO_4 /ACN solution.

Polarization curves, carried out on various dyed TiO_2 thin films and a bare TiO_2 as a comparison, were recorded by means of CV from 0 V to -0.5 V Vs SCE in 10^{-2} M I⁻/ 10^{-2} M I_2 /ACN solution. The applied voltage (Φ) was reported against the logarithm of the current density for Tafel analysis.

Photocurrent density-voltage (J/V) curves were recorded with a PGSTAT 302N potentiostat equipped with an ABET sun simulator and an AM1.5G filter by setting the spectral irradiance to 100 mW/cm^2 (1 SUN). Cells were placed on a black opaque holder to avoid the back scattering of the transmitted light. The Incident Photon to Current Conversion Efficiency (IPCE%) spectra were collected with a homemade apparatus composed by a Xenon lamp (Ceralux CL300BF) and a National Instrument PXI 1033 measurements system under short circuit conditions. The Absorbed Photon to Current Conversion Efficiency (APCE%) spectra were calculated according to APCE%

= IPCE%/LHE (Light Harvesting Efficiency), the latter parameter was extrapolated by the absorption spectra of the dyed TiO₂ recorded in transmission mode against an undyed TiO₂ as reference, according to $LHE = 1 - 10^{-A(\lambda)}$. The absorption spectra were corrected for the bathochromic shift originated by the intercalation into the mesoporous TiO₂ film of the small high-density cations by using a shape factor obtained by the ratio of the normalized spectra recorded when the titania films were in the presence and in the absence of the lithium cations.³ Steady state spectroelectrochemistry was carried out on the same sensitized thin transparent TiO₂ used for transient absorption spectroscopy (see below) by applying a positive polarization in the range 0.28-1.18 v vs Fc⁺/Fc in ACN/0.1 M LiClO₄ (Reference: Ag wire, counter electrode: Pt wire). Spectra were reported in difference mode, by considering the spectral variations with respect to the open circuit conditions (disconnected wires).

Transient Absorption Spectroscopy (TAS) of the Fe(II)NHC sensitized transparent TiO₂ films were obtained with a Nd:YAG laser (Continuum Surelite II) and a monochromatic probe beam. The thin FTO slides were held at 45° to both the laser beam and the monochromatic probe beam to scatter the laser light away from the photomultiplier tube (PMT). To increase the signal-to-noise-ratio (S/N) multiple shots (ca. 50) were accumulated and the signal was pre-amplified with different impedances (varying to 350 Ω to 1 M Ω) selected on the bases of the time scale set for the experiments. The Fe(II)NHC sensitized thin films were in contact with 0.1M LiClO₄/ACN solution or with a blank electrolyte (deprived of I⁻ and I₂) (0.1 M LiOTf, 0.6 M PMIOtf, 0.1 M GuNCS, 0.1 M TBAPF₆, 0.1 MgOTf₂) or with the reduced form or the electrolyte (deprived of I₂) (0.1 M LiI, 0.6 M PMII, 0.1 MgI₂, 0.1 M GuNCS, 0.1 M TBAI). The contact between the dyed Titania films and the electrolyte were realized by pressing a glass slide to the active side of the sensitized semiconductor and by filling the created gap by capillarity with the solution of interest.¹

Absorption spectra of electrodes

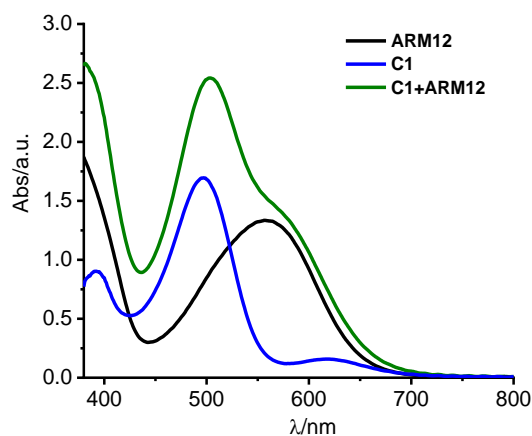


Figure S20: Sequences obtained for the realization of the co-sensitization.

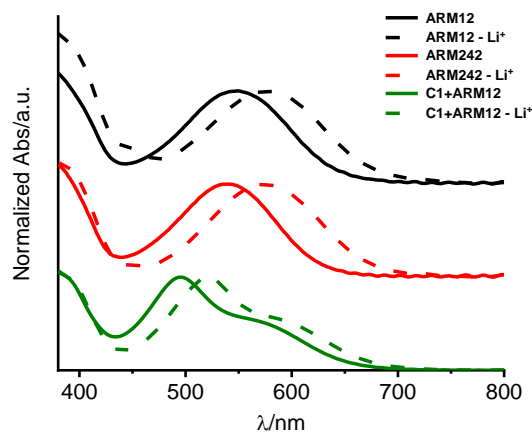


Figure S21: Absorption spectra of the sensitized TiO_2 in contact with air (solid line) and with 0.1M $\text{LiClO}_4/\text{ACN}$ solution (dashed line).

Transient spectroscopy

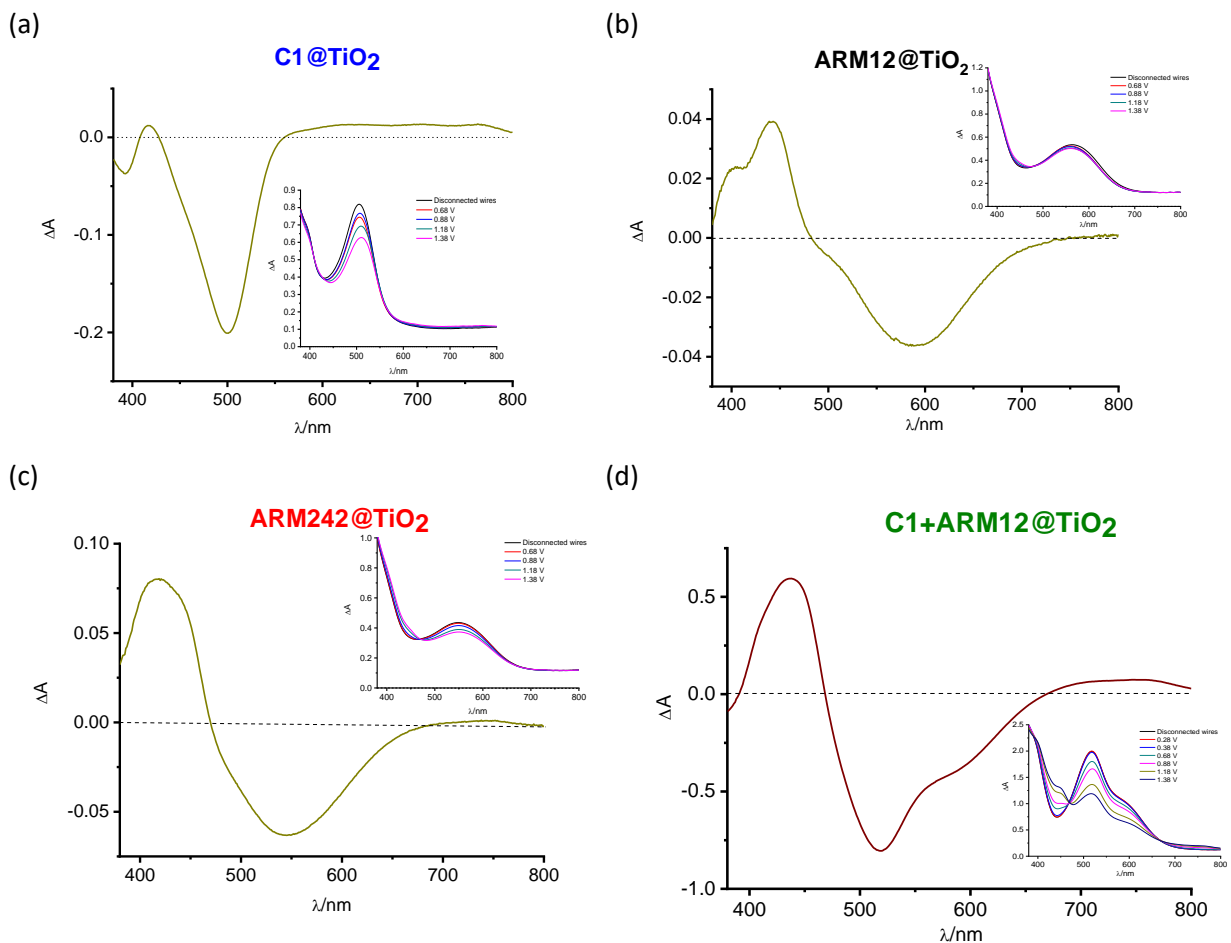


Figure S22: Difference absorption spectra (ΔA vs λ) of dye/ TiO_2 films measured in a three-electrode spectroelectrochemical cell in 0.1 M/ACN electrolyte. The inserts show the change in the absorption spectra of the dyes following positive polarization from open circuit (disconnected wires) up to +1.38 V Vs Fc^+/Fc .

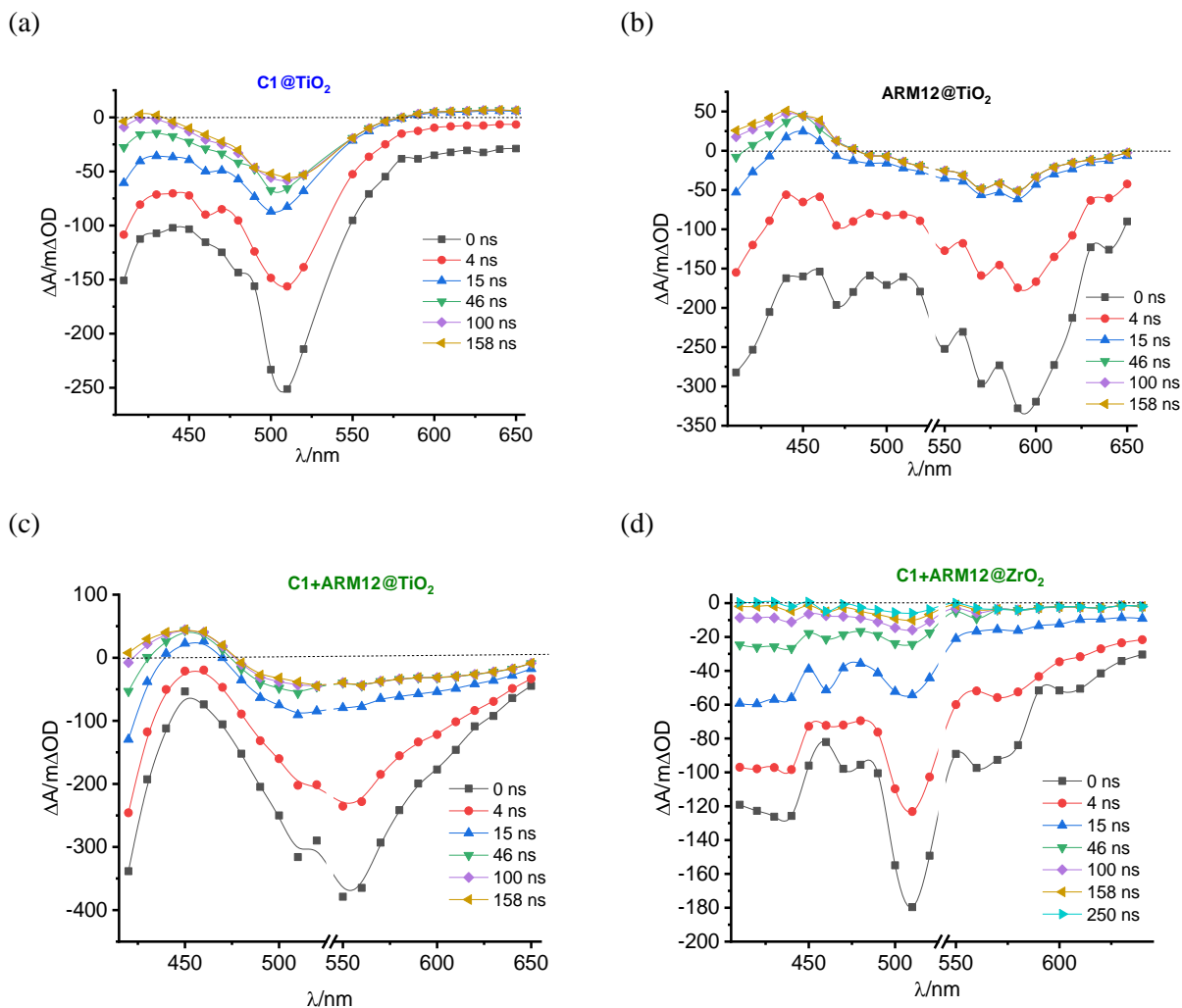


Figure S23: Transient Absorption Spectra at early delays for: (a-c) for **C1**, **ARM12** and the **C1+ARM12** loaded on TiO_2 and (d) **C1+ARM12** loaded on ZrO_2 . Input impedance: 50 Ω . Laser Power: 30 $mJ/cm^2/pulse$. λ_{exc} : 355 nm.

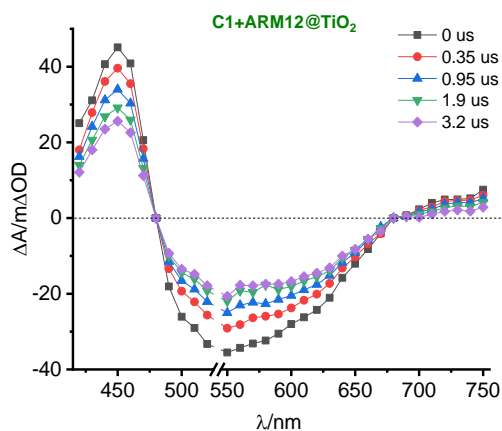


Figure S24: Transient absorption spectra recorded for the **C1+ARM12** with 355 nm laser excitation. Laser power: 20 $mJ/cm^2/pulse$. Input impedance: 350 Ω .

Photovoltaic properties

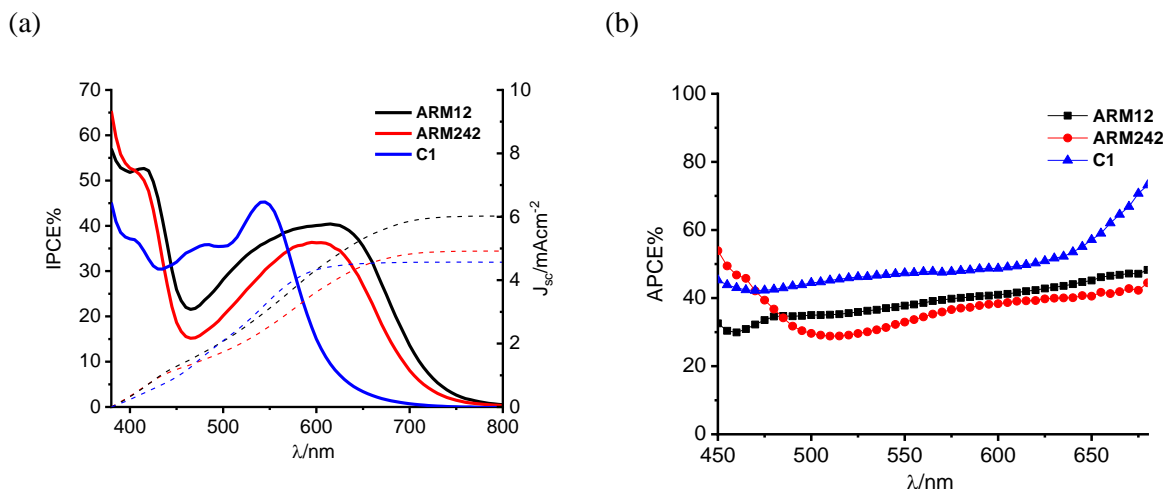


Figure S25: (a) Incident Photon to Current Conversion Efficiency spectra for the Fe(II)NHC sensitized TiO₂ with a 13 μm Films. The dashed line represents the short circuit integrated photocurrent. (b) Absorbed Photon to Current Conversion Efficiency spectra for Fe(II)NHC sensitized TiO₂ computed by the point (a) according to $APCE = IPCE/LHE$.

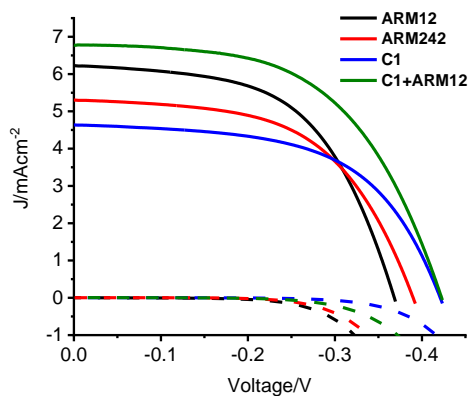


Figure S26: Photocurrent Density – Voltage curves for the Fe(II)NHC sensitized cells based on 13 μm thick TiO₂.

Table S11: Relevant parameters for the Fe(II)NHC complexes loaded on 13 μm thick TiO₂ films.

Complex	J _{sc} / (mA/cm ²)	V _{oc} / V	FF%	η%
ARM12	6.23±0.41	0.37±0.02	56±1	1.28±0.14
ARM242	5.30±0.17	0.39±0.02	55±3	1.14±0.10
C1	4.64±0.25	0.42±0.01	57±2	1.11±0.09
C1+ARM12	6.78±0.28	0.42±0.02	55±2	1.56±0.16

References

- 1 A. Reddy Marri, E. Marchini, V. D. Cabanes, R. Argazzi, M. Pastore, S. Caramori and P. C. Gros, *J. Mater. Chem. A*, 2021, **9**, 3540–3554.
- 2 Y. Liu, T. Harlang, S. E. Canton, P. Chábera, K. Suárez-Alcántara, A. Fleckhaus, D. A. Vithanage, E. Göransson, A. Corani, R. Lomoth, V. Sundström and K. Wärnmark, *Chem. Commun.*, 2013, **49**, 6412.
- 3 A. R. Marri, E. Marchini, V. D. Cabanes, R. Argazzi, M. Pastore, S. Caramori, C. A. Bignozzi and P. C. Gros, *Chem. – Eur. J.*, 2021, **27**, 16260–16269.
- 4 M. Pastore, T. Duchanois, L. Liu, A. Monari, X. Assfeld, S. Haacke and P. C. Gros, *Phys Chem Chem Phys*, 2016, **18**, 28069–28081.
- 5 M. Reiher, *Inorg. Chem.*, 2002, **41**, 6928–6935.
- 6 I. M. Dixon, G. Boissard, H. Whyte, F. Alary and J.-L. Heully, *Inorg. Chem.*, 2016, **55**, 5089–5091.
- 7 L. A. Fredin, M. Pápai, E. Rozsályi, G. Vankó, K. Wärnmark, V. Sundström and P. Persson, *J. Phys. Chem. Lett.*, 2014, **5**, 2066–2071.
- 8 K. P. Kepp, *Inorg. Chem.*, 2016, **55**, 2717–2727.
- 9 A. D. Becke, *J. Chem. Phys.*, 1993, **98**, 5648–5652.
- 10 J. Tomasi, B. Mennucci and R. Cammi, *Chem. Rev.*, 2005, **105**, 2999–3094.
- 11 Gaussian 16, Revision C.01, M. J. Frisch, G. W. Trucks, H. B. Schlegel, G. E. Scuseria, M. A. Robb, J. R. Cheeseman, G. Scalmani, V. Barone, G. A. Petersson, H. Nakatsuji, X. Li, M. Caricato, A. V. Marenich, J. Bloino, B. G. Janesko, R. Gomperts, B. Mennucci, H. P. Hratchian, J. V. Ortiz, A. F. Izmaylov, J. L. Sonnenberg, D. Williams-Young, F. Ding, F. Lipparini, F. Egidi, J. Goings, B. Peng, A. Petrone, T. Henderson, D. Ranasinghe, V. G. Zakrzewski, J. Gao, N. Rega, G. Zheng, W. Liang, M. Hada, M. Ehara, K. Toyota, R. Fukuda, J. Hasegawa, M. Ishida, T. Nakajima, Y. Honda, O. Kitao, H. Nakai, T. Vreven, K. Throssell, J. A. Montgomery, Jr., J. E. Peralta, F. Ogliaro, M. J. Bearpark, J. J. Heyd, E. N. Brothers, K. N. Kudin, V. N. Staroverov, T. A. Keith, R. Kobayashi, J. Normand, K. Raghavachari, A. P. Rendell, J. C. Burant, S. S. Iyengar, J. Tomasi, M. Cossi, J. M. Millam, M. Klene, C. Adamo, R. Cammi, J. W. Ochterski, R. L. Martin, K. Morokuma, O. Farkas, J. B. Foresman, and D. J. Fox, Gaussian, Inc., Wallingford CT, 2016.
- 12 M. Pastore, A. Selloni, S. Fantacci and F. De Angelis, in *First Principles Approaches to Spectroscopic Properties of Complex Materials*, eds. C. Di Valentin, S. Botti and M. Cococcioni, Springer Berlin Heidelberg, Berlin, Heidelberg, 2014, vol. 347, pp. 1–45.
- 13 S. Grimme, J. Antony, S. Ehrlich and H. Krieg, *J. Chem. Phys.*, 2010, **132**, 154104.
- 14 J. P. Perdew, K. Burke and M. Ernzerhof, *Phys. Rev. Lett.*, 1997, **78**, 1396–1396.
- 15 A. Klamt and G. Schüürmann, *J Chem Soc Perkin Trans 2*, 1993, 799–805.
- 16 G. te Velde, F. M. Bickelhaupt, E. J. Baerends, C. Fonseca Guerra, S. J. A. van Gisbergen, J. G. Snijders and T. Ziegler, *J. Comput. Chem.*, 2001, **22**, 931–967.
- 17 I. Kondov, M. Čížek, C. Benesch, H. Wang and M. Thoss, *J. Phys. Chem. C*, 2007, **111**, 11970–11981.
- 18 G. Di Carlo, S. Caramori, V. Trifiletti, R. Giannuzzi, L. De Marco, M. Pizzotti, A. Orbelli Biroli, F. Tessore, R. Argazzi and C. A. Bignozzi, *ACS Appl. Mater. Interfaces*, 2014, **6**, 15841–15852.
- 19 E. Marchini, S. Caramori, R. Boaretto, V. Cristino, R. Argazzi, A. Niorettini and C. A. Bignozzi, *Appl. Sci.*, 2021, **11**, 2769.